In Situ X-ray imaging of HT-PEMFC hot-pressing using contrast enhancement

Adam Zucconi [a,b], Jennifer Hack [a], Theo A.M. Suter [a], Michele Braglia [b], Paul R. Shearing [a],
Dan J.L. Brett [a], Alexander J.E. Rettie [a,*]

[a] *Electrochemical Innovation Lab, Department of Chemical Engineering, UCL, London WC1E 7JE, UK*
[b] *Mobility Innovation Hub, HORIBA MIRA, Nuneaton, Warwickshire, CV10 0TU, UK*

HIGHLIGHTS

- *In situ* radiography of phosphoric acid penetration in HT-PEMFCs.
- Novel contrast agent method to improve phosphoric acid visualisation.
- Quantification of phosphoric acid in GDLs using X-ray computed tomography.
- Analysis of effects of hot-press pressure, duration, and compression on distribution.
- High pressure and lack of compression gasket led to most significant penetration.

ARTICLE INFO

ABSTRACT

A contrast enhancement agent is used to visualise phosphoric acid penetration and distribution in high-temperature polymer electrolyte membrane fuel cells. This new method is demonstrated in the investigation of hot-pressing parameters on phosphoric acid penetration and distribution. *In situ* radiography of the hot-press process showed acid plumes breaking through the catalyst layer, microporous layer (MPL) and gas diffusion layer (GDL). The phosphoric acid volume and distribution within the MPL and GDL are quantified, and their dependence on hot-press pressure, duration and compression control are analysed. Increasing hot-press pressure and duration was found to increase acid penetration and delamination of the membrane and catalyst layers. The absence of a compression control gasket also led to significant infiltration into the MPL and GDL. Penetration occurred first at the anode for all tests, which was attributed to a higher number of cracks and greater degree of crack connectivity. Phosphoric acid entered the MPL and GDL either through initial breakthrough of the catalyst layer, or from acid pooling on the GDL surface and being compressed into the fibres. This work provides a novel method to improve visualisation of phosphoric acid and highlights the acid loss mechanisms resulting from hot-press conditions.

1. Introduction

Polymer electrolyte membrane fuel cells (PEMFCs) are expected to play a key role in the decarbonisation of transportation, heating and power, and already have an established presence in markets such as materials handling and remote/back-up power [1–3]. However, issues of expensive membrane and catalyst materials, complex water management, extreme sensitivity to fuel impurities and poor heat rejection still remain [4–6]. High-temperature (HT) PEMFCs offer multiple advantages over the more mature low-temperature (LT) technology; these include faster reaction kinetics, increased tolerance

of platinum catalyst to fuel impurities, and simplified water and thermal management [7–11]. HT-PEMFCs most commonly use phosphoric acid (PA)-doped membranes due to the high proton conductivity under anhydrous conditions that is characteristic of PA [12]. Despite the benefits of PA, its migration and loss is an important degradation mechanism that affects cell performance and long-term durability [13,14]. Phosphoric acid must be distributed within the catalyst layers to provide sufficient proton conduction and catalyst utilisation [14]. However, the acid can be permanently lost when it penetrates through the catalyst layers into the microporous and gas diffusion layers, and

out to flow fields [15]. When the acid is lost, this degradation mechanism reduces the content of the main proton conductor, which affects the charge transfer impedance, ohmic resistance and durability of the fuel cell [16]. Also, the acid within the porous diffusion structures impedes flow of the reactants to the active sites, increasing mass transport resistance [17]. Therefore, developing an understanding of acid distribution within HT-PEMFCs is crucial to improve acid management and enhance performance over extended periods of time.

The desire to visualise PA in HT-PEMFCs is similar to that of water in LT-PEMFCs. Methods that have been used to successfully visualise water include optical and infrared imaging [18–20], environmental scanning electron microscope (ESEM) [21], neutron imaging and scattering [22–24], and magnetic resonance imaging [25,26]. One of the most powerful and useful techniques to study internal structures and dynamics of PEMFCs non-destructively is X-ray computed tomography (X-ray CT) and radiography. These techniques have been used to conduct *operando* studies to visualise water in 3 and 4D [27–29].

Similarly, X-ray CT and radiography have been used to investigate the distribution of PA in HT-PEMFCs. Initial *operando* studies used X-ray radiography to identify water and PA in an operating HT-PEMFC [30–32]. Eberhardt et al. [33] used synchrotron-based X-ray CT to determine the distribution and concentration of PA in the membrane electrode assembly (MEA) of a non-operating HT-PEMFC. The method to identify PA relied on calibration curves relating the greyscale value to known concentrations of PA. Later, the same group used synchrotron-based X-ray CT to study PA migration in operating cells [15,34,35]. This allowed for the visualisation of PA migration from cathode to anode during operation, which was found to increase with current density and acid doping level [35]. Bevilacqua and Halter et al. both used synchrotron- and lab-based studies to investigate PA migration through the catalyst layer, microporous layer (MPL), and gas diffusion layer (GDL) [13,17,36]. The studies revealed that increased catalyst layer crack width, connectivity, and overlap with MPL cracks results in greater PA penetration into the diffusion layers, and that the MPL plays an important role in redistributing PA in the catalyst layer and inhibiting leaching. This is in agreement with work by Chevalier et al. which used pore network modelling to investigate the impact of the MPL on PA redistribution, and found that the MPL acted as a barrier to contain PA in the void regions of the catalyst layer [37].

Analysis of X-ray CT datasets typically involves segmentation of the components of interest. In order to segment the PA, Bevilacqua and Halter et al. used a reference subtraction method whereby the electrode is imaged prior to assembly or testing [13,17,36]. This is to allow a "dry" dataset to be subtracted from the dataset containing PA ("wet") to distinguish the acid. This method is required due to the similarity in greyscale values between PA and the surrounding carbon materials and voids in the diffusion layers. The issue with this method is that it adds complexity and is time-consuming as it necessitates additional scans and image processing; it also limits the scope of studies as the electrode must be imaged prior to the introduction of PA. If the electrode morphology changed sufficiently (e.g. under compression), then subtraction would not be suitable. Bailey et al. used machine learning to assist the segmentation process of PA for lab-based X-ray CT datasets of HT-PEMFCs [38]. Despite the successful segmentation of PA using lab-based instruments, the requirement for additional "dry" scans and user input still leaves work to be done to improve PA identification and analysis in X-ray CT and radiography studies.

This work provides a new technique to improve PA visualisation and segmentation when using X-ray CT or radiography to image HT-PEMFCs. The technique uses a contrast-enhancing agent or "tracer", a technique that is common in medical applications of X-ray imaging [39], and has been applied to batteries [40], and to PEMFC GDLs [41]. The aim of using the tracer is to provide sufficient contrast such that additional "dry" datasets are not required, thus reducing the experimental time and complexity of analysis. To illustrate the effectiveness of the new method, *in situ* imaging of hot-pressing that

would not be possible using the subtraction method is conducted. The effects of hot-pressing conditions have been investigated for LT-PEMFCs [42–44], but there is little on this topic for HT-PEMFCs. Although HT-PEMFCs can be assembled in the cell without prior hot-pressing, hot-pressing is still commonly used and will impact the morphology of the membrane, catalyst layers, and diffusion layers. It is also a mechanism for PA loss [45].

Here, the contrast enhancement technique allows for *in situ* radiographic imaging of the hot-press process, and allows for simplified post-hot-press image processing and analysis of the CT datasets.

2. Materials and methods

2.1. Membrane electrode assembly

The membrane and electrodes used in this study are the commercially available Celtec PA doped-polybenzimidazole (PBI) membrane, P1100 anode and P1100 cathode produced by BASF (Germany). The electrodes consist of a woven carbon fibre GDL, MPL, and Pt and Pt-alloy catalyst layers at the anode and cathode, respectively. Prior to scanning, the electrodes and membrane were cut into 3 mm diameter circles using a laser micro-machining tool (A Series/Compact System, Oxford Lasers, UK). The electrodes and membrane were then assembled into a bespoke sample holder, described in detail in Section 2.3.

2.2. Contrast enhancement

A caesium compound was chosen to act as the contrast agent/tracer, specifically caesium sulphate (Cs_2SO_4, 99.99%, Sigma-Aldrich, USA). This was chosen due to the atomic number, Z, of Cs being considerably higher than that of hydrogen, carbon, oxygen, and phosphorous which are typically found in the MPL and GDL and possess similar greyscale values. The relative intensities of the transmitted X-rays give rise to contrast in the image. The transmitted X-ray intensity is given in Eq. (1):

$$I = I_0 e^{(\mu/\rho)\rho x} \tag{1}$$

where I and I_0 are the transmitted and incident X-ray intensities respectively, μ/ρ is the mass attenuation coefficient (linear attenuation coefficient/material density), and x is the material thickness. The linear attenuation coefficient is dependent on the photon interaction through the photoelectric and Compton interactions:

$$\mu_{Total} = \mu_{Photoelectric} + \mu_{Compton} \tag{2}$$

Photoelectric attenuation dominates in the photon energy range that is typically used for lab-based X-ray CT [46]. The contrast enhancement agent makes use of the dependence of the probability of the photoelectric absorption on the atomic number of the attenuating medium:

$$P(\text{photoelectric absorption}) \sim \frac{Z^3}{E^3} \tag{3}$$

where E is the photon energy. The mass attenuation coefficients of elements found in a HT-PEMFC along with Cs are shown in Supplementary Figure S1. The attenuation coefficients of H, C, and P are relatively close in the range of photon energy used in typical lab-based X-ray CT (30–150 keV); and the value for Cs is significantly higher and thus should provide good contrast through higher attenuation. The values for Cs and Pt are similar, which may affect the contrast between these elements. However, the difference in Cs and Pt material density meant that this was not a significant issue in this work, and the focus of this study is to easily distinguish the PA from the diffusion layers.

Cs was also chosen due to its analogous Cs^+ ion to H^+ so as to enable ion exchange reactions, whereby Cs_3PO_4, Cs_2HPO_4, and CsH_2PO_4 are expected to be produced and act as the tracer compounds. The exact ion exchange reaction and conversion rate was not determined, but
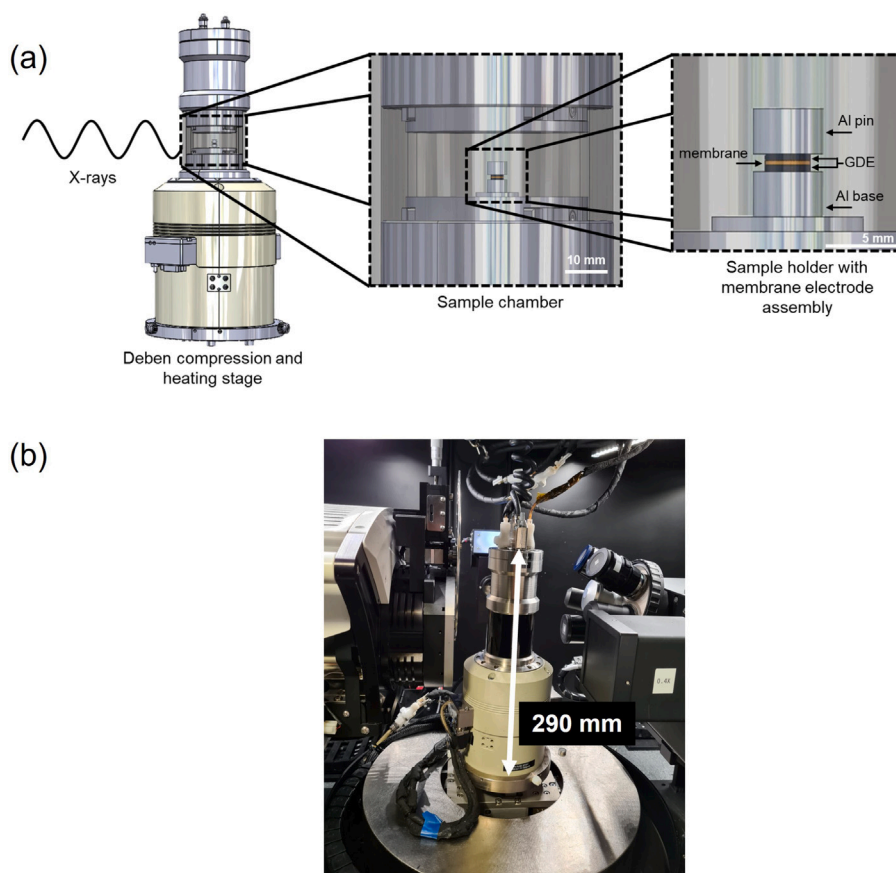
Fig. 1. (a) Diagram of Deben compression and heating stage with sample holder, and (b) photograph of setup.

sulphur compounds will also be produced. Multiple masses of Cs_2SO_4 were assessed for contrast enhancement for the hot-pressing study, and the results are shown in Supplementary Figure S2. High levels of the Cs compound prevented dissolution in the deionised (DI) water and formed a surface layer on the membrane, although the surface layer appears negligible at typical hot-press and HT-PEMFC operating temperatures. Low levels led to insufficiently enhanced contrast. The optimised concentration of Cs_2SO_4 was determined to be 1250 $mg_{Cs_2SO_4}/ml_{DI}$ and deposited onto the membrane of area 12.25 cm^2 using a glass pipette, covering the whole surface. The membrane was then placed within a hot-press (without contact on the upper/deposited surface of the membrane) for 90 s at 140 °C, a Kapton sheet was then placed over the membrane and continued to be heated at 140 °C for another 90 s. This was expected to be sufficient time to allow the ion exchange process to occur and evaporate the water from the surface of the membrane.

2.3. Sample holder and compression stage

To recreate the hot-pressing process and allow for *in situ* imaging, a Deben CT5000 stage (Deben UK Ltd, UK) was used to apply compression and heating and controlled by Microtest software. The stage consisted of sample chamber between a fixed upper platen, and moveable lower platen which was used to control the compression. The sample chamber and holder are shown magnified in Fig. 1(a). The temperature of the upper and lower platens of the stage are controlled independently and were set to the desired hot-press pressure before the hot-press procedure. The sample holder was designed and manufactured to hold the electrodes and membrane in place for scanning

and hot-pressing. This consisted of an aluminium base and pin, which the MEA was placed between. A Kapton sheath was placed around the sample holder to prevent misalignment, and a Kapton disc was positioned between the surface of each GDE and the Al pin or base to prevent the MEA sticking to the aluminium. A Kapton gasket was placed around the MEA to control compression. The full setup is shown in Fig. 1, the sheath and gasket are omitted so that the MEA can be seen. The hot-press parameters for each test are given in Section 2.6. The electrodes and membrane were assembled into the sample holder using a benchtop optical microscope to achieve the component alignment before entering the compression stage prior to the first scan.

2.4. X-ray computed tomography and radiography

Imaging was conducted using a laboratory X-ray CT system, ZEISS Xradia 520 Versa with tungsten as the target metal (Carl Zeiss, USA). The sample sizes used were 3 mm discs, this size was selected as a balance between X-ray penetration and thus signal-to-noise, and representative area. This sample size is expected to not result in significant differences compared to larger area MEAs typically used for electrochemical operation, and is therefore representative. This is justified due to the same hot-press conditions (temperature, force/area, and duration) used for both types of MEA size. The acid pathways through the catalyst and microporous layers should be the same regardless of sample size used for imaging, and the crack dimensions will not change due to using smaller lateral sample areas. Also, the thickness of the MEA does not change when the lateral sample area is reduced.

One 3D scan was conducted prior to hot-pressing, another 3D scan was conducted after the hot-press process. Pre-hot-press scans were
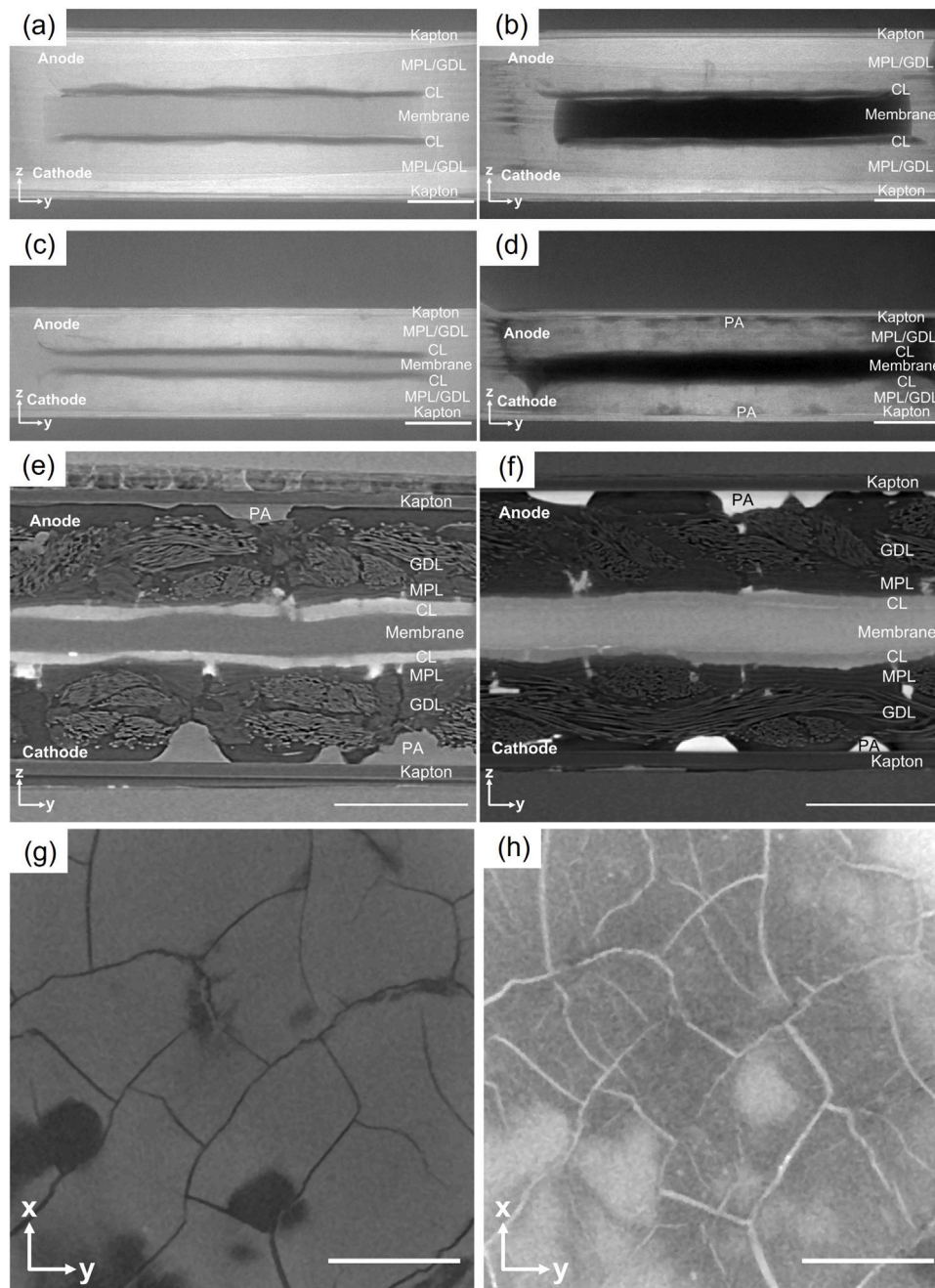
Fig. 2. Comparison of tracer effect on contrast and detection of PA. Radiographs: (a) hot-press start - no tracer (b) hot-press start - with tracer, (c) hot-press end - no tracer, and (d) hot-press end - with tracer. Orthoslices of 3D reconstructed datasets: (e) no tracer and (f) with tracer. Cathode cracks and PA visualisation: (g) before hot-press and (h) after hot-press. All scale bars are 500 μm.

conducted at 25 °C. Post-hot-press scans were conducted at 130 °C. These scans used a source voltage of 80 kV, exposure time of 8 s, 4× magnification, and consisted of 1201 projections. A binning of 2 was selected to allow for a reduced exposure time and thus scan time due to the high number of tests. The hot-pressing process was imaged as a series of radiographs. This is because it is a dynamic process occurring in 3 min or less, therefore, the flux and exposure times of lab-based systems are not capable of capturing this process in 3D. The radiography was conducted using a higher source voltage of 100 kV. This was done to increase the average photon count, allowing the exposure time to be reduced to 0.5 s. The magnification used was 4×. These imaging parameters gave a pixel and voxel (volume pixel) dimension of 3.5 μm with a field of view of approximately 3.4 mm for all tests.

2.5. Image processing and analysis

2.5.1. Tomography

The reference-corrected radiographs were reconstructed using XMReconstructor software (Carl Zeiss, USA). The remaining processing and analyses were conducted in Avizo software (Thermo Fisher Scientific, USA). A subvolume was extracted from the 3D dataset for analysis. The dimensions of the subvolume were 500 × 500 × 400 voxels, giving a volume of 4.34 mm^3. Previous studies using similar X-ray CT setups determined the representative elementary area (minimum area required to be representative of a larger volume) of a PEMFC to be 0.10–0.36 mm^2 [43,47]; this compares to ~3 mm^2 in this study. Therefore, the volume analysed was deemed to be representative of

Table 1
Hot-pressing parameters used in this study.

Test identifier	Temperature (°C)	Pressure (N mm^{-2})	Hold duration (s)	Compression (%)
1 (*baseline*)	130	4	30	25
2 (*P*: 2)	130	2	30	25[a]
3 (*P*: 8)	130	8	30	25[a]
4 (*D*: 180)	130	4	180	25
5 (*C*: 50)	130	4	30	50
6 (*C*: UnC)	130	4	30	Uncontrolled

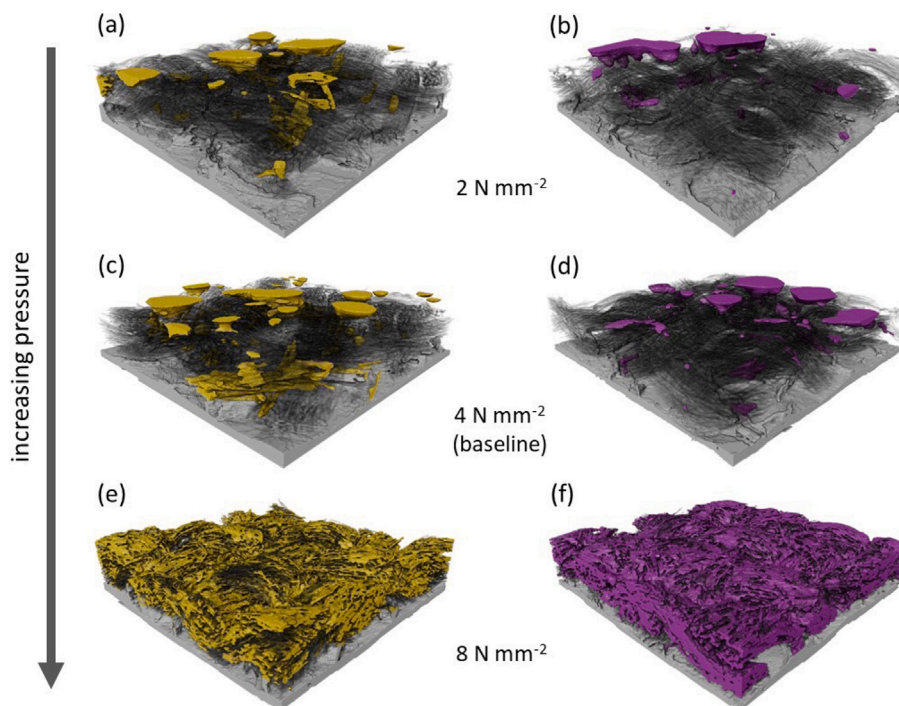[a] Compression control relative to baseline pressure (4 N mm^{-2}).

Fig. 3. Volume renderings of the electrodes comparing results of hot-press pressure. Test 2: 2 N mm^{-2}, (a) anode, (b) cathode. Test 1: 4 N mm^{-2}, (c) anode, (d) cathode. Test 3: 8 N mm^{-2}, (e) anode, (f) cathode. The anode and cathode PA are false coloured yellow and purple, respectively. The fibres are presented with reduced opacity to enable PA penetration to be visible, and the catalyst layer is light grey. The sample rendering length and width are both 1.76 mm. (For interpretation of the references to colour in this figure legend, the reader is referred to the web version of this article.)

the larger sample. A variation of non-local means and median filters were applied to the first dataset to determine the optimum processing. A filter procedure of 3 iterations of XY plane median filtering was chosen and applied to all datasets after the subvolume extraction. Segmentation of the datasets based on differences in greyscale was achieved using a combination of "Threshold" and "Magic Wand" functions in the Avizo software. The volume of PA in the MPL and GDL, and the volume fraction profile of PA distribution were evaluated using MATLAB software (Mathworks, USA) to process the segmented data.

2.5.2. Radiography

After reference correction, the individual radiographs required alignment. This was achieved using a combination of the "landmark alignment" and "least-squares alignment" modes in Avizo's "Align Slices" module. The datasets were then cropped to remove the majority of the aluminium sample holder. The radiographs were then compiled into videos using Fiji (ImageJ) software.

2.6. Hot-pressing

After the pre-hot-press scan, the sample and holder were removed from the stage, and the stage was heated to test temperature. This was done to replicate how MEAs are hot-pressed for electrochemical operation whereby the components are placed into the press only once it has reached the desired temperature. The scan was started and the desired force was set to be applied and maintained at a constant load. The compression jaw motor speed was 1 mm s^{-1}. After pressing, the compression stage jaws were opened such that load was no longer applied to the MEA. The hot-pressing parameters are shown in Table 1, the identifiers "*P*", "*D*", and "*C*" refer to pressure, duration and compression respectively. Test 1 parameters are a baseline. Tests 2 and 3 are used to determine the effect of hot-press pressure. Test 4 has an increased hot-press duration hold at the specified pressure. To determine the impact of a gasket to control compression, test 5 has a thinner hard-stop allowing for 50% compression compared to the baseline 25%, and test 6 does not use a hardstop and the compression was not controlled. Hot-press temperature has been shown to affect LT-PEMFCs as the temperatures used are close to the glass transistion temperature of the perfluorosulphonic acid (PFSA) membranes [43]. Typical hot-press temperatures for HT-PEMFCs are 130–200 °C [48–51]; and thus are not close to the glass transition temperature of PBI (425–436 °C) [52]. This, combined with the temperature limitations of the stage (∼ 150 °C) meant that the effect of hot-press temperature was not investigated in this work.

The workflow from membrane preparation to post-hot press scan is shown in Supplementary Figure S3.
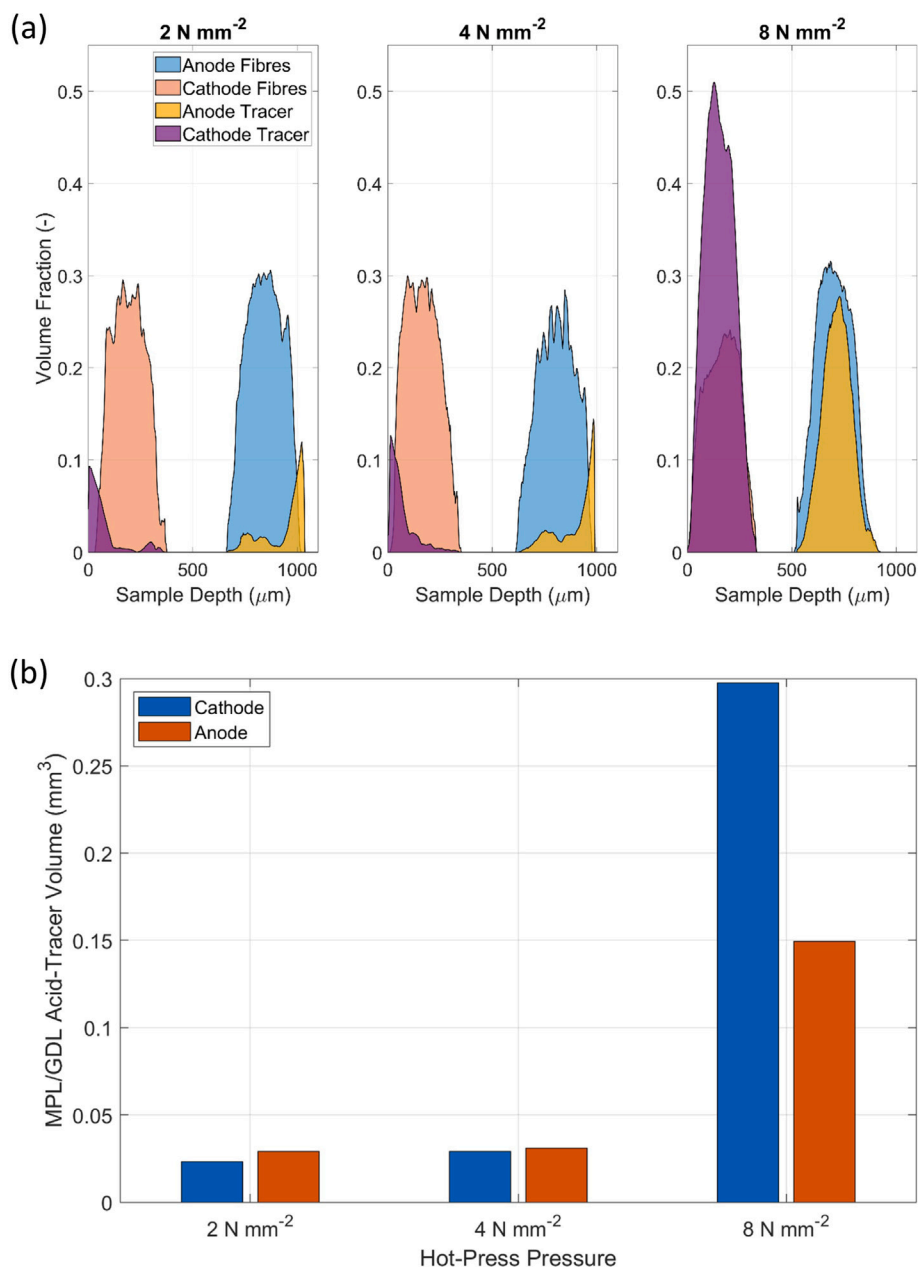
Fig. 4. Effect of hot-press pressure on (a) volume fraction depth profile of acid in MPL and GDL, and (b) total volume of acid in MPL and GDL.

3. Results and discussion

3.1. Evaluation of contrast agent

Fig. 2 shows the effect of the contrast tracer on the hot-press radiography and reconstructed tomograms. The radiography without and with the tracer can be seen in Supplementary Video SV1 and SV2, respectively. The tracer clearly allows for visualisation of PA penetration into the MPL and GDL during the hot-press process. The greyscale intensities of the orthoslices in Fig. 2e and f show the effect of the tracer allowing for PA to be easily distinguished from the catalyst layers, MPL, GDL and void volume - allowing for simplified segmentation, which is not the case in studies requiring the subtraction segmentation method to distinguish carbon materials from PA [13,35,36,38]. The tracer also allows for the penetration into the cracks to be seen as shown in the images of the cathode catalyst layer before and after hot-pressing (Figs. 2g and 2h respectively). PA can be seen penetrating through cracks in the post-hot-press image that are not visible in the

pre-hot-press image. This suggests that additional cracks may form during hot-pressing through which PA can penetrate into the MPL and GDL.

3.2. Hot-press pressure

The radiography videos of the hot-press process in Supplementary Videos SV2, SV3, and SV4 show how the PA penetration occurred as a function of time. Due to the constant motor speed throughout tests, the time taken to reach the hot-press pressure increased as the pressure target set point increased. Radiographs of the first point of PA penetration, 10 s prior to the hold ($t - 10$), the point at which the target pressure is reached ($t = 0$), and at the end of the hold ($t + 30$) are shown in Supplementary Figures S4, S5, and S6. The first signs of PA penetration occurred at the anodes at approximately 14, 19 and 30 s before the target pressure is reached for tests 2 (*P*: 2), 1 (*P*: 4), and 3 (*P*: 8) respectively. The radiographs indicate that a significant quantity of PA has penetrated before the start of the pressure hold, with
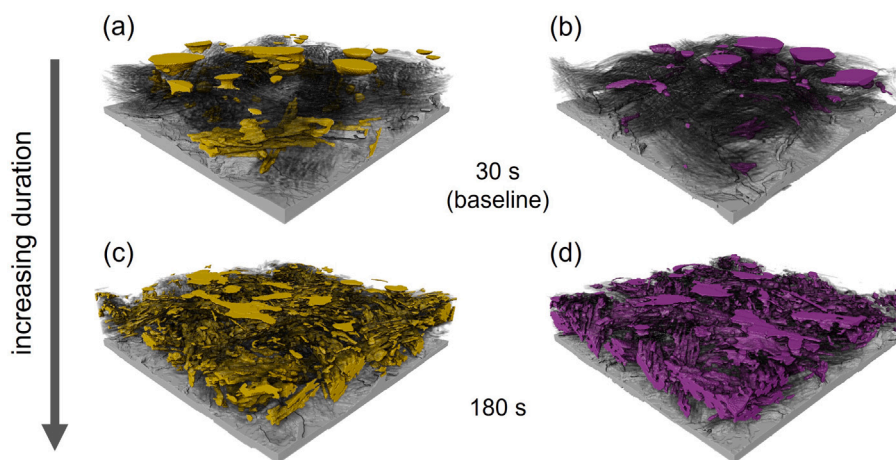
Fig. 5. Volume renderings of the electrodes comparing results of hot-press duration. Test 1: 30 s, (a) anode, (b) cathode. Test 4: 180 s, (c) anode, (d) cathode. The anode and cathode PA are false coloured yellow and purple, respectively. The fibres are presented with reduced opacity to enable PA penetration to be visible, and the catalyst layer is light grey. The sample rendering length and width are both 1.76 mm. (For interpretation of the references to colour in this figure legend, the reader is referred to the web version of this article.)

plumes and pools of PA visible in both electrodes. The breakthrough of the PA into the catalyst layer and up through the MPL and GDL relies on overlapping catalyst layer and MPL cracks which provide pathways for the PA to enter the GDL [17]. Cracks in the MPL are typically in the tens of microns and can be up to 150 μm, and PA will migrate along the MPL and enter the GDL through these cracks [17,36]. These breakthrough events are clearly visible in the radiography videos as plumes of PA erupt through the catalyst layer and infiltrate the MPL and GDL.

Volume renderings of the PA distribution resulting from different hot-press pressures are shown as plural renderings in Fig. 3. These images containing segmented PA, fibres and catalyst layers, as well as the radiography videos (SV2, SV3, and SV4) indicate a clear and significant increase in PA penetration as hot-press pressure increased from 2 N mm^{-2} to 4 N mm^{-2} to 8 N mm^{-2}. This is attributed to a greater degree of compression of the PA-doped membrane as hot-press pressure increases, and a greater amount of PA is forced out through cracks in the catalyst layer.

It was observed that both the volume of PA that penetrates the fibres and the distribution is influenced by pressure (Fig. 4). For test 1 (*P*: 4) and test 2 (*P*: 2), the volume of PA penetrated is higher for the anode than cathode (0.031 mm^3 compared to 0.029 mm^3, and 0.029 mm^3 compared to 0.023 mm^3 for tests 1 (*P*: 4) and 2 (*P*: 2), respectively). A similar result was found by Halter et al. who observed greater PA breakthrough at the anode during operation when using MEA materials similar to those used in this study [17]. An explanation for this may be the increased number of cracks and degree of connectivity at the anode which is visible in the 3D datasets. These parameters have been identified as important factors in PA redistribution [13]. The thinner cracks at the anode can result in higher capillary pressure, which increases PA invasion and branching [36]. These parameters may also explain the penetration occurring at the anode first for all tests. However, the volume of PA was higher in the cathode than anode for test 3 (*P*: 8) (0.298 mm^3 and 0.149 mm^3, respectively). Orthoslices of the anode and cathode catalyst layers are shown in Supplementary Figure S7 to indicate the greater number of thinner cracks at the anode. However, the resolution in the study is not sufficient to accurately measure crack widths and volumes at the anode quantitatively in order to confirm its effect, and therefore should be investigated in future work.

The distribution of PA was similar for test 1 (*P*: 4) and 2 (*P*: 2), with the volume fraction of PA peaking at the GDL surface (Fig. 4a). The PA was found to adhere to the Kapton sheets contacting the GDL surfaces and protrude into the fibres. The adhesion forces are noticable when the Kapton sheets are removed from the MEA and carry the

surface PA with them, leaving the GDL surface relatively dry of acid (shown in Supplementary Figure S8). As the pressure increases, the volume fraction of PA within the GDL interior increases. This is evident in Figs. 3 and 4a where almost all the PA that has penetrated in test 3 (*P*: 8) is contained within the fibre volume; suggesting the adhesion forces to the Kapton were overcome and the fibres became saturated. The saturation effect is so severe that the segmentation of the PA from the fibres was difficult, and likely led to a slight underestimation of the fibre volume. The fibre saturation means that PA would not be removed along with the Kapton sheet, and removal via wicking when gases are supplied during operation would be challenging due to the high volume of PA blocking gas pathways. Interestingly, the distribution of PA within both electrodes favoured containment within the GDL with minimal PA confined to the MPL, reasons for this include increased porosity and void spaces in the GDL to store PA, and the "acidophobic" nature of PTFE within the MPL [13]. However, the PTFE loading in the MPL and GDL used in this work is proprietary information and thus its influence on this effect is not clear.

The change in MEA thickness as a result of the hot-press pressure is shown in Table 2. The decrease in thickness increased with pressure (−21%, −25%, and −30% for tests 2 (*P*: 2), 1 (*P*: 4), and 3 (*P*: 8) respectively). It should be noted that the pressure in test 3 (*P*: 8) was sufficiently high to cause the gasket to compress notably such that the total compression exceeded 25%, likewise test 2 (*P*: 2) compression was slightly less than 25%. The fibres suffered the greatest compression, followed by the membrane, and the catalyst layer thickness changed the least as a result of hot-press pressure. The level of delamination was assessed qualitatively from the 3D datasets, and was noted to increase with hot-press pressure. Test 2 (*P*: 2) exhibited almost no delamination, whilst test 1 (*P*: 4) had some limited disconnect between the catalyst layers and membrane close to the edges of the selected volume, and test 3 (*P*: 8) resulted in significant delamination across the width of the membrane. These results show that excessive pressures cause high volumes of PA to be lost from the membrane, significant blockage of

Table 2
Hot-press pressure effect on average MEA thicknesses.

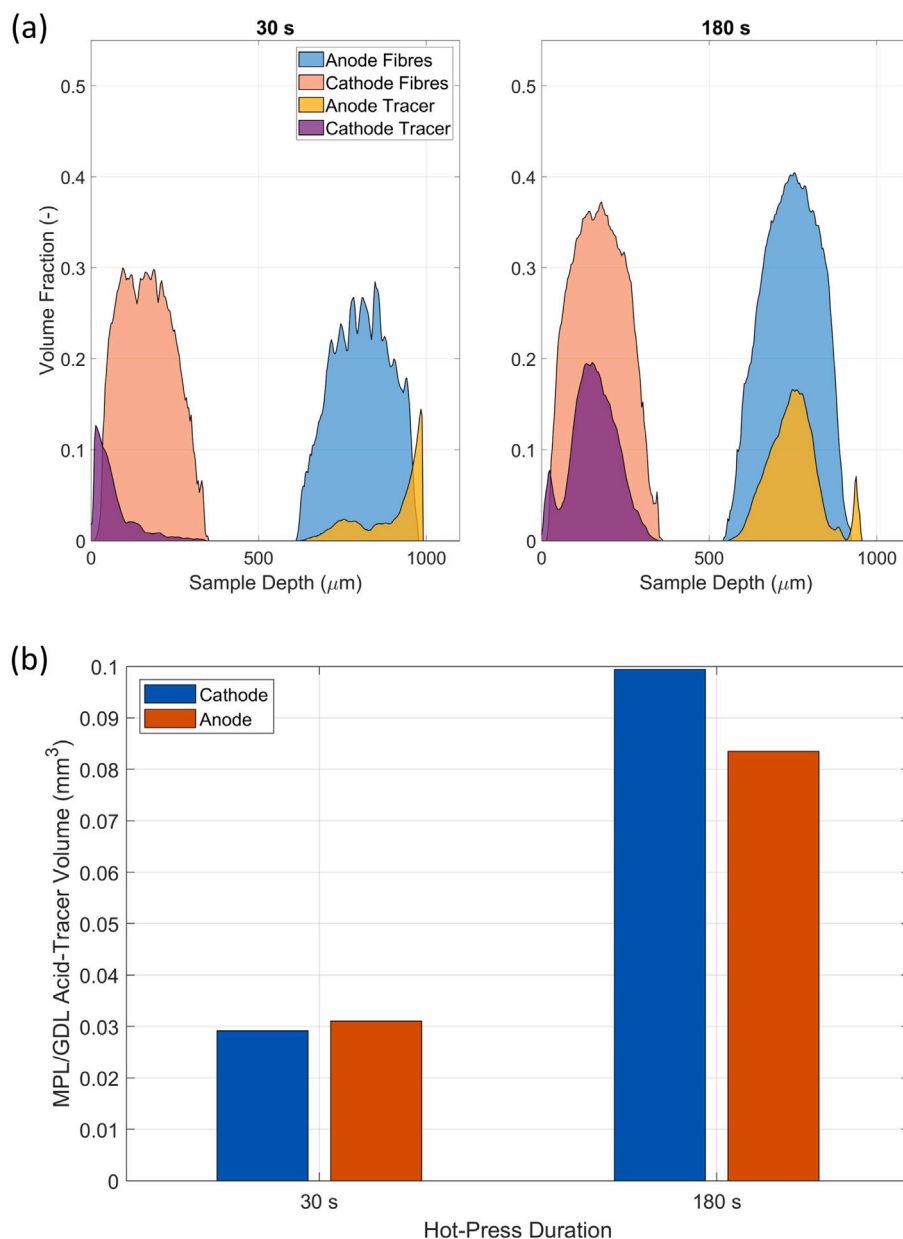| Hot-press pressure (N mm^{-2})	Thickness (before) (μm)	Thickness (after) (μm)	Change (%)
2	1175	928	−21
4	1212	910	−25
8	1196	842	−30

Fig. 6. Effect of hot-press duration on (a) volume fraction depth profile of acid in MPL and GDL, and (b) total volume of acid in MPL and GDL.

diffusion layers, and poor contact between the membrane and catalyst layers.

3.3. Hot-press duration

The impact of duration on the hot-press process as a function of time is visible when comparing the radiograph videos shown in Supplementary Videos SV2 and SV5. Despite the temperature, pressure, duration, and compression being the same up to the first 30 s of the hold, the radiographs (Supplementary Figures S4 and S9) show that test 4 (*D*: 180) has a greater amount of PA in the diffusion layers at *t*=0. Considering the parameters and compression gasket were the same, the difference could potentially be explained by electrode morphology differences. Despite these differences, the effect of duration can still be inferred. The radiographs show that there is a clear increase in PA penetration between 30 and 180 s. This increased saturation of the diffusion layers over time is clearly visible in the radiographs where a darkening of the layers can be seen (Supplementary Figures S4 and S9). The first plumes of acid penetrating the catalyst layer occur at the

anode, which is the same as the pressure tests. Some of the plumes appear to intrude a short distance, potentially blocked by the MPL or GDL. Whereas multiple plumes can be seen penetrating the catalyst layer and reaching the GDL surface. Once at the surface, the volume of PA is compressed and begins to move back into the fibres. This results in PA penetration into the GDL and MPL from both directions, firstly PA which has been forced through the catalyst layer, and secondly PA at the GDL surface being compressed back into the fibres.

The volume renderings of the electrodes post-hot-press are shown in Fig. 5, and there is a clear increase in PA penetration into the GDL when the duration is increased. The distribution of the PA in test 4 (*D*: 180) (Fig. 6a) is more similar to that of the high-pressure test (test 3 (*P*: 8), Fig. 4a). While there is some PA pooling at the surface of the GDL as in test 1 and 2, the majority is contained within the diffusion layer interior. Similarly to the other tests, the MPL contains very little PA and this is attributed to smaller pores, limited void space, and potentially greater PTFE loading. The volume of PA in the anode and cathode of test 4 (*D*: 180) was 0.083 mm^3 and 0.099 mm^3 respectively,
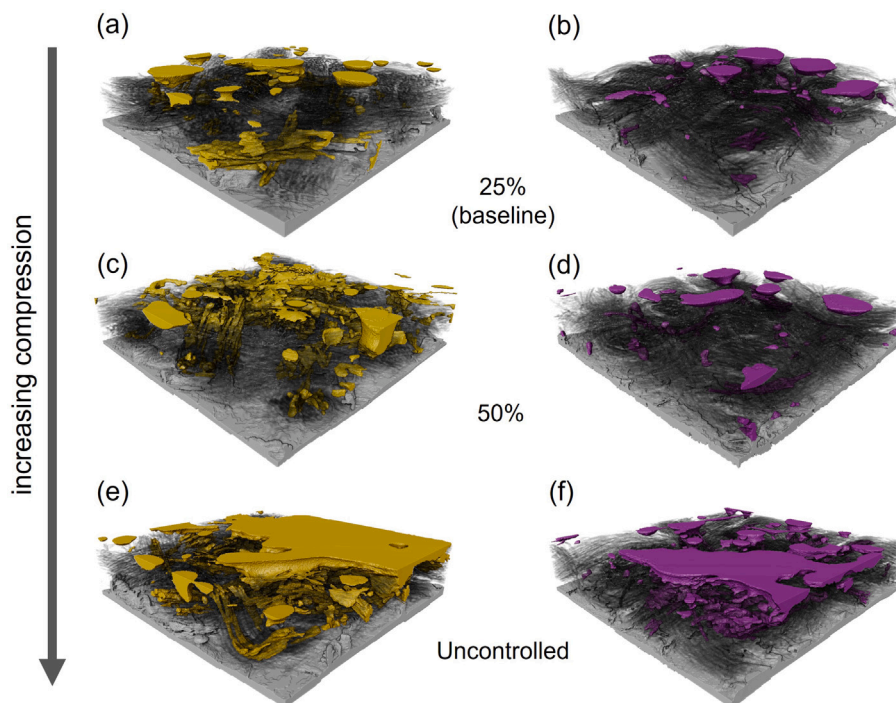
Fig. 7. Volume renderings of the electrodes comparing results of hot-press compression. Test 1: 25% (a) anode, (b) cathode. Test 5: 50%, (c) anode, (d) cathode. Test 6: uncontrolled, (e) anode, (f) cathode. The anode and cathode PA are false coloured yellow and purple, respectively. The fibres are presented with reduced opacity to enable PA penetration to be visible, and the catalyst layer is light grey. The sample rendering length and width are both 1.76 mm. (For interpretation of the references to colour in this figure legend, the reader is referred to the web version of this article.)

Table 3
Hot-press duration effect on average MEA thicknesses.

Hot-press duration (s)	Thickness (before) (μm)	Thickness (after) (μm)	Change (%)
30	1212	910	−25
180	1199	854	−29

compared to 0.031 mm^3 and 0.029 mm^3 for test 1 (*D*: 30) respectively (Fig. 6(b)).

Test 4 (*D*: 180) is also the only test other than test 3 (*P*: 8) to result in a greater volume of acid in the cathode than anode at the end of the hot-press process (Fig. 6b). This suggests that duration may have a greater impact on the penetration into the cathode, as in all tests the first sign of penetration occurs at the anode, yet the two longest duration tests result in higher final volume in the cathode. An explanation could be that greater pressure is required at the cathode for the PA to penetrate, and the longer duration allows time for this pressure to build. This could be attributed to the lower number of cracks and crack connectivity at the cathode resulting in fewer penetration pathways.

The change in MEA thickness is shown in Table 3. A greater decrease in MEA thickness is seen in test 4 (*D*: 180) (−29%), suggesting duration does affect this parameter. The membrane is thinner at the end of test 4 (*D*: 180) than test 1 (*D*: 30), and the higher PA loss from the membrane is a likely cause of this shrinking. The increased duration led to an increase in the levels of delamination between the catalyst layers and membrane; however, this was not as severe test 3 (*P*: 8).

3.4. Hot-press compression

A Kapton compression gasket was used to control the compression of the MEA to 25% and 50% in tests 1 (*C*: 25) and 5 (*C*: 50) respectively, and test 6 (*C*: UnC) has no gasket so that the compression is uncontrolled. The radiography videos for these tests are shown

in Supplementary Videos SV2, SV6, and SV7. The videos show that penetration once again occurs first at the anode, and plumes of PA are clearly seen moving out through the catalyst layers and into the MPLs, GDLs, and to the GDL surfaces. The radiographs for tests 1 (*C*: 25), 5 (*C*: 50), and 6 (*C*: UnC) are shown in Supplementary Figures S4, S10 and S11 respectively. As the hold begins at *t* = 0, the PA that has penetrated appears to increase with increasing compression. This is expected as a higher level of compression will result in reduced membrane volume, and thus an increase in the PA pressure exerted on the catalyst layer, resulting in more penetration. The radiographs at end of the hold (*t*+ 30) show that PA levels at the surfaces of the GDL and within the GDLs has increased. This supports the evidence in the other tests that PA continues to penetrate the MPL and GDL in both directions during the hold despite a constant temperature, compression and pressure applied by the hot-press unit.

The volume renderings are shown in Fig. 7. A greater PA content in the anode compared to the anode is visible in the volume renderings. Test 6 (*C*: UnC) shows significant pooling of PA on the GDL surfaces, as well as high PA content within the fibres. The PA that leached out of the sides of the membrane and adhered to the Kapton surfaces did not result in as much PA penetration from the surface of the GDL into the fibres as with the other tests. Instead, the PA appears to pool at the MEA edges which is shown in the volume renderings and radiography. The lack of penetration despite the large volume of PA pooling here may be explained by a lack of pathways for the PA to move through due to the high degree of compression i.e., the void spaces in the GDL are greatly reduced.

The PA content within the fibres generally increased with compression: 0.031 mm^3 and 0.029 mm^3, 0.067 mm^3 and 0.020 mm^3, and 0.181 mm^3 and 0.062 mm^3 for the anode and cathode of tests 1 (*C*: 25), 5 (*C*: 50), and 6 (*C*: UnC), respectively (Fig. 8b). Higher volumes of PA were found in the anode for all tests, and the distribution of the PA is shown in Fig. 8a. As with the other tests, the MPL contains very little PA.
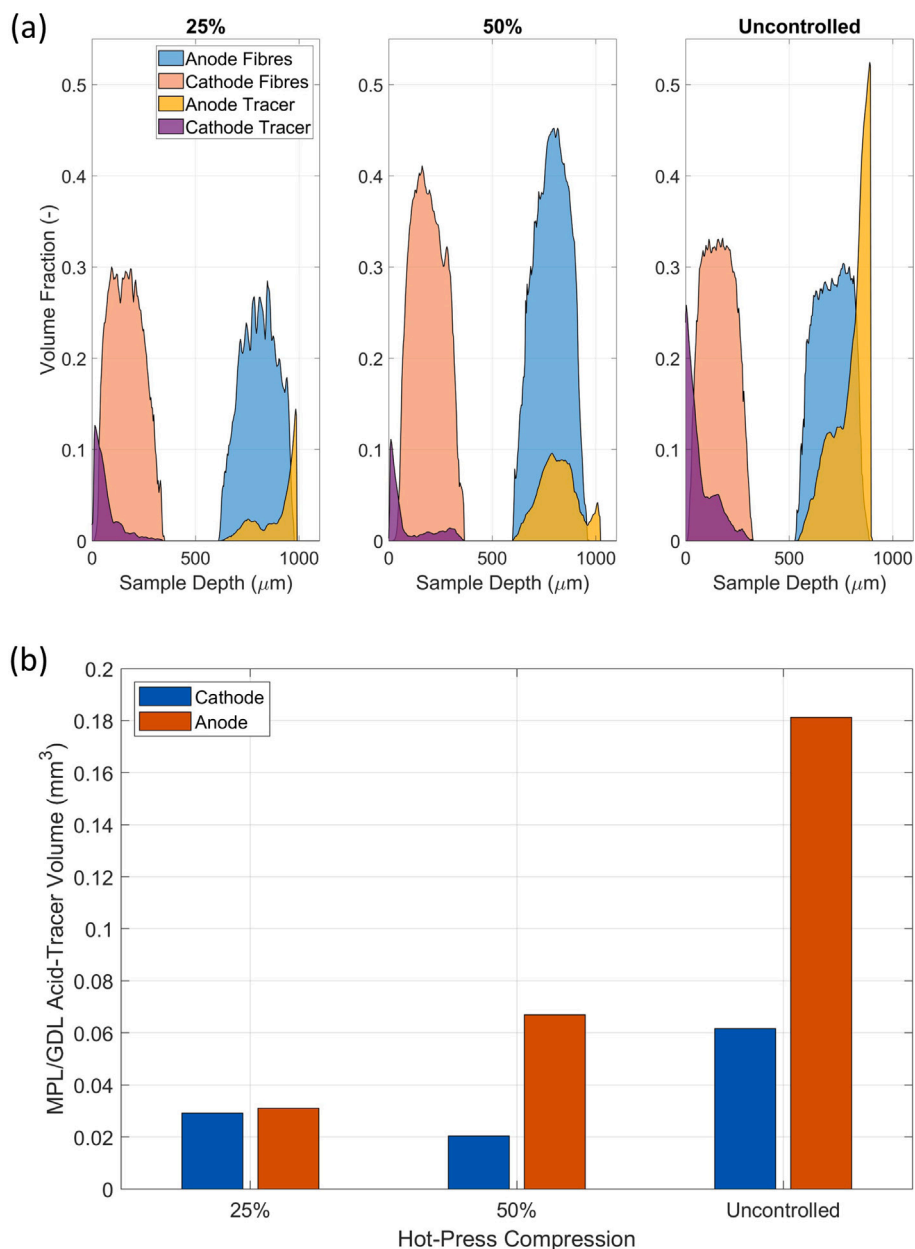
Fig. 8. Effect of compression control on (a) volume fraction depth profile of acid in MPL and GDL, and (b) total volume of acid in MPL and GDL.

Interestingly, the total volume of PA at the cathode is lower for test 5 (*C*: 50) than test 1 (*C*: 25) (Fig. 8b). This is unexpected and once again highlights the potential impact of another parameter that is not considered in this study such as electrode morphology. However, the increase in PA at the cathode for test 5 (*C*: 50), and the further increase at both cathode and anode when compression is uncontrolled, clearly show the importance of compression in PA penetration during hot-pressing.

The average MEA thickness decreased with increasing compression as shown in Table 4. This follows the trend in the pressure and duration tests whereby higher PA loss from the membrane results in a thinner membrane and overall thickness decrease. The thickness changes were −25%, −30%, and −32% for tests 1 (*C*: 25), 5 (*C*: 50), and 6 (*C*: UnC), respectively. Despite the differences in MEA thicknesses, all three tests showed similarly low levels of delamination. However, a tear in the membrane was present after the uncontrolled compression in test 6 (*C*: UnC) which may have been caused by the larger membrane deformation resulting from a lack of compression control.

Table 4
Hot-press duration effect on average MEA thicknesses.

Hot-press compression (%)	Thickness (before) (µm)	Thickness (after) (µm)	Change (%)
25	1212	910	−25
50	1251	873	−30
Uncontrolled	1178	805	−32

4. Conclusions

This study demonstrated the use of a contrast agent as a PA tracer in HT-PEMFC X-ray imaging. Difficulties in distinguishing PA within the catalyst layers, MPL, and GDL is overcome using a Cs compound to increase the X-ray attenuation of the PA-tracer mixture, and subsequently increase contrast. The enhanced contrast eliminates the need for additional scanning such as in the subtraction method used to track PA, and

allows for simple and fast segmentation. The usefulness of the contrast enhancement method is highlighted using an *in situ* hot-pressing study on the effects of pressure, duration, and compression control on the distribution of PA within the electrodes. Dynamic visualisation of the PA penetrating the catalyst layer, MPL, and GDL was captured using X-ray radiography. X-ray CT allowed for 3D visualisation of the PA within the MEA and quantification of the PA volume and distribution within the MPL/GDL.

Increasing hot-press pressure and duration resulted in greater PA penetration and delamination, whilst also causing a reduction in the membrane and average MEA thickness. Compression control also had a significant impact on the PA penetration and distribution. Uncontrolled compression led to large volumes of PA pooling on the GDL surface, as well as the greatest reduction in MEA thickness. The hot-press pressure of 8 N mm^{-2} resulted in the highest volume of PA penetration at the cathode and anode (0.298 mm^3 and 0.149 mm^3 respectively). At this pressure, the fibres became saturated with PA.

The radiography showed that PA penetration always occurred first at the anode, and this was attributed to a greater number of cracks and increased connectivity at the anode compared to the cathode. PA entered the GDL and MPL via two pathways: the first through PA forced through the catalyst layer and trapped in these layers, the second through PA which has pooled on the GDL surface and is compressed into the GDL. Minimal PA was contained within the MPL and this was attributed to reduced pore size and void space compared to the GDL, and potentially greater "acidophobic" effect caused by higher PTFE loading in the MPL. PA penetration and distribution within the MEA continued with time despite constant pressure, compression, and temperature once the hold point was reached. The results highlight hot-pressing as a PA loss mechanism, as well as the importance of optimising hot-press parameters for HT-PEMFCs to minimise unnecessary PA penetration and blockage of diffusion pathways that would require removal during conditioning, while maintaining good contact between the catalyst layer and membrane.

The use of the contrast agent offers a new way to enhance contrast in imaging of PA in HT-PEMFCs. Future development of this method should focus on the optimisation of the agent itself as well as the quantity. A relatively high concentration was used in this study which is partly due to the compromises in imaging parameters required when using the heating and compression stage. Lower levels can be used when there is greater freedom to optimise the source and detector distances. Application of the agent into MEAs could also be used for enhanced PA tracking in *operando* and *ex situ* studies, although the effect on fuel cell performance should also be considered.

This work offers a new method for visualising PA in HT-PEMFCs X-ray imaging, and enables *in situ* studies with simplified segmentation due to the enhanced contrast between PA and the other materials. The hot-pressing study identified the acid loss pathways during pressing, and highlighted the importance of optimising pressure and duration, as well as the utilisation of a compression gasket to avoid excessive acid loss.

CRediT authorship contribution statement

Adam Zucconi: Conceptualisation, Methodology, Investigation, Formal analysis, Data curation, Validation, Visualisation, Writing – original draft, Project administration. **Jennifer Hack:** Investigation, Formal analysis, Writing – review & editing. **Theo A.M. Suter:** Methodology, Investigation. **Michele Braglia:** Writing – review & editing. **Paul R. Shearing:** Supervision & provision of equipment. **Dan J.L. Brett:** Writing – review & editing, Supervision. **Alexander J.E. Rettie:** Writing – review & editing, Supervision.

Declaration of competing interest

The authors declare that they have no known competing financial interests or personal relationships that could have appeared to influence the work reported in this paper.

Data availability

The authors do not have permission to share data.

Acknowledgements

Appendix A. Supplementary data

Supplementary material related to this article can be found online at https://doi.org/10.1016/j.jpowsour.2023.233574.

References

[1] Yun Wang, Hao Yuan, Andrew Martinez, Patrick Hong, Hui Xu, Fred R. Bockmiller, Polymer electrolyte membrane fuel cell and hydrogen station networks for automobiles: Status, technology, and perspectives, Adv. Appl. Energy (ISSN: 26667924) 2 (December 2020) (2021) 100011, http://dx.doi.org/10.1016/j.adapen.2021.100011.

[2] Iain Staffell, Daniel Scamman, Anthony Velazquez Abad, Paul Balcombe, Paul E. Dodds, Paul Ekins, Nilay Shah, Kate R. Ward, The role of hydrogen and fuel cells in the global energy system, Energy Environ. Sci. (ISSN: 17545706) 12 (2) (2019) 463–491, http://dx.doi.org/10.1039/c8ee01157e.

[3] Gareth Hinds, In situ diagnostics for polymer electrolyte membrane fuel cells, Curr. Opin. Electrochem. (ISSN: 24519111) 5 (1) (2017) 11–19, http://dx.doi.org/10.1016/j.coelec.2017.08.010.

[4] Guoqiang Li, Wojciech Kujawski, Edyta Rynkowska, Advancements in proton exchange membranes for high-performance high-temperature proton exchange membrane fuel cells (HT-PEMFC), Rev. Chem. Eng. (ISSN: 0167-8299) (2020) 87–100, http://dx.doi.org/10.1515/revce-2019-0079.

[5] Timothy Myles, Leonard Bonville, Radenka Maric, Catalyst, membrane, free electrolyte challenges, and pathways to resolutions in high temperature polymer electrolyte membrane fuel cells, Catalysts (ISSN: 2073-4344) 7 (12) (2017) 16, http://dx.doi.org/10.3390/catal7010016, URL http://www.mdpi.com/2073-4344/7/1/16.

[6] R.E. Rosli, A.B. Sulong, W.R.W. Daud, M.A. Zulkifley, T. Husaini, M.I. Rosli, E.H. Majlan, M.A. Haque, A review of high-temperature proton exchange membrane fuel cell (HT-PEMFC) system, Int. J. Hydrogen Energy (ISSN: 03603199) 42 (14) (2017) 9293–9314, http://dx.doi.org/10.1016/j.ijhydene.2016.06.211.

[7] Susanta K. Das, Antonio Reis, K.J. Berry, Experimental evaluation of CO poisoning on the performance of a high temperature proton exchange membrane fuel cell, J. Power Sources (ISSN: 03787753) 193 (2) (2009) 691–698, http://dx.doi.org/10.1016/j.jpowsour.2009.04.021.

[8] Venkatesh Babu Venkatesh, Geethu Varghese, Thadathil Varghese Joseph, Purushothama Chippar, Spatial analysis of CO poisoning in high temperature polymer electrolyte membrane fuel cells, Int. J. Hydrogen Energy (ISSN: 03603199) 46 (11) (2021) 8179–8196, http://dx.doi.org/10.1016/j.ijhydene.2020.12.001.

[9] Amrit Chandan, Mariska Hattenberger, Ahmad El-Kharouf, Shangfeng Du, Aman Dhir, Valerie Self, Bruno G. Pollet, Andrew Ingram, Waldemar Bujalski, High temperature (HT) polymer electrolyte membrane fuel cells (PEMFC)-A review, J. Power Sources (ISSN: 03787753) 231 (2013) 264–278, http://dx.doi.org/10.1016/j.jpowsour.2012.11.126.

[10] Chaojie Song, Yanghua Tang, Jian Lu Zhang, Jiujun Zhang, Haijiang Wang, Jun Shen, Scott McDermid, Jing Li, Paul Kozak, PEM fuel cell reaction kinetics in the temperature range of 23–120 °C, Electrochim. Acta (ISSN: 00134686) 52 (7) (2007) 2552–2561, http://dx.doi.org/10.1016/j.electacta.2006.09.008.

[11] Jianlu Zhang, Yanghua Tang, Chaojie Song, Jiujun Zhang, Polybenzimidazole-membrane-based PEM fuel cell in the temperature range of 120–200 °C, J. Power Sources (ISSN: 03787753) 172 (1) (2007) 163–171, http://dx.doi.org/10.1016/j.jpowsour.2007.07.047.

[12] Erli Qu, Xiaofeng Hao, Min Xiao, Dongmei Han, Sheng Huang, Zhiheng Huang, Shuanjin Wang, Yuezhong Meng, Proton exchange membranes for high temperature proton exchange membrane fuel cells: Challenges and perspectives, J. Power Sources (ISSN: 03787753) 533 (August 2021) (2022) 231386, http://dx.doi.org/10.1016/j.jpowsour.2022.231386.

[13] J. Halter, N. Bevilacqua, R. Zeis, T.J. Schmidt, F.N. Büchi, The impact of the catalyst layer structure on phosphoric acid migration in HT-PEFC – An operando X-ray tomographic microscopy study, J. Electroanal. Soc. (ISSN: 15726657) 859 (2020) 113832, http://dx.doi.org/10.1016/j.jelechem.2020.113832.

[14] A. Kannan, Q. Li, L.N. Cleemann, J.O. Jensen, Acid distribution and durability of HT-PEM fuel cells with different electrode supports, Fuel Cells (ISSN: 16156846) 18 (2) (2018) 103–112, http://dx.doi.org/10.1002/fuce.201700181, URL http://doi.wiley.com/10.1002/fuce.201700181.

[15] S.H. Eberhardt, M. Toulec, F. Marone, M. Stampanoni, F.N. Büchi, T.J. Schmidt, Dynamic operation of HT-PEFC: In-operando imaging of phosphoric acid profiles and (re)distribution, J. Electrochem. Soc. (ISSN: 0013-4651) 162 (3) (2015) F310–F316, http://dx.doi.org/10.1149/2.0751503jes.

[16] Yeon Hun Jeong, Kyeongmin Oh, Sungha Ahn, Na Young Kim, Ayeong Byeon, Hee Young Park, So Young Lee, Hyun S. Park, Sung Jong Yoo, Jong Hyun Jang, Hyoung Juhn Kim, Hyunchul Ju, Jin Young Kim, Investigation of electrolyte leaching in the performance degradation of phosphoric acid-doped polybenzimidazole membrane-based high temperature fuel cells, J. Power Sources (ISSN: 03787753) 363 (2017) 365–374, http://dx.doi.org/10.1016/j.jpowsour.2017.07.109.

[17] J. Halter, F. Marone, T.J. Schmidt, F.N. Büchi, Breaking through the cracks: On the mechanism of phosphoric acid migration in high temperature polymer electrolyte fuel cells, J. Electrochem. Soc. (ISSN: 0013-4651) 165 (14) (2018) F1176–F1183, http://dx.doi.org/10.1149/2.0501814jes.

[18] M.M. Daino, Z. Lu, J.M. LaManna, J.P. Owejan, T.A. Trabold, S.G. Kandlikar, Through-plane water transport visualization in a PEMFC by visible and infrared imaging, Electrochem. Solid-State Lett. (ISSN: 10990062) 14 (6) (2011) B51, http://dx.doi.org/10.1149/1.3560163, URL https://iopscience.iop.org/article/10.1149/1.3560163.

[19] M.I. Rosli, D.J. Borman, D.B. Ingham, M.S. Ismail, L. Ma, M. Pourkashanian, Transparent PEM fuel cells for direct visualization experiments, J. Fuel Cell Sci. Technol. (ISSN: 1550624X) 7 (6) (2010) 1–7, http://dx.doi.org/10.1115/1.4001353.

[20] A. Bazylak, D. Sinton, Z.S. Liu, N. Djilali, Effect of compression on liquid water transport and microstructure of PEMFC gas diffusion layers, J. Power Sources (ISSN: 03787753) 163 (2) (2007) 784–792, http://dx.doi.org/10.1016/j.jpowsour.2006.09.045.

[21] R. Alink, D. Gerteisen, W. Mérida, Investigating the water transport in porous media for PEMFCs by liquid water visualization in ESEM, Fuel Cells (ISSN: 16156846) 11 (4) (2011) 481–488, http://dx.doi.org/10.1002/fuce.201000110.

[22] Kanae Ito, Takeshi Yamada, Akihiro Shinohara, Shin-ichi Takata, Yukinobu Kawakita, Dynamics of water in a catalyst layer of a fuel cell by quasielastic neutron scattering, J. Phys. Chem. C (ISSN: 1932-7447) 125 (39) (2021) 21645–21652, http://dx.doi.org/10.1021/acs.jpcc.1c06014, URL https://pubs.acs.org/doi/10.1021/acs.jpcc.1c06014.

[23] A. Putra, H. Iwase, D. Yamaguchi, S. Koizumi, Y. Maekawa, M. Matsubayashi, T. Hashimoto, In-situ observation of dynamic water behavior in polymer electrolyte fuel cell by combined method of Small-Angle Neutron Scattering and Neutron Radiography, J. Phys. Conf. Ser. (ISSN: 1742-6596) 247 (2010) 012044, http://dx.doi.org/10.1088/1742-6596/247/1/012044, URL https://iopscience.iop.org/article/10.1088/1742-6596/247/1/012044.

[24] P. Boillat, E.H. Lehmann, P. Trtik, M. Cochet, Neutron imaging of fuel cells – Recent trends and future prospects, Curr. Opin. Electrochem. (ISSN: 24519103) 5 (1) (2017) 3–10, http://dx.doi.org/10.1016/j.coelec.2017.07.012, URL https://linkinghub.elsevier.com/retrieve/pii/S2451910317300236.

[25] S. Tsushima, T. Ikeda, T. Koido, S. Hirai, Investigation of water distribution in a membrane in an operating PEMFC by environmental MRI, J. Electrochem. Soc. (ISSN: 00134651) 157 (12) (2010) B1814, http://dx.doi.org/10.1149/1.3486168, URL https://iopscience.iop.org/article/10.1149/1.3486168.

[26] Toshikazu Kotaka, Shohji Tsushima, Shuichiro Hirai, Visualization of membrane hydration path in an operating PEMFC by nuclei-labeling MRI, ECS Trans. (ISSN: 1938-5862) 11 (1) (2007) 445–450, http://dx.doi.org/10.1149/1.2780958, URL https://iopscience.iop.org/article/10.1149/1.2780958.

[27] Jooyoung Park, Hwanyeong Oh, Hanwook Park, Jong Woon Moon, Sang Joon Lee, Sang Yong Jung, Water transport in polymer electrolyte membrane fuel cell: Degradation effect of gas diffusion layer, Int. J. Energy Res. (ISSN: 0363-907X) 46 (7) (2022) 9058–9070, http://dx.doi.org/10.1002/er.7782, URL https://onlinelibrary.wiley.com/doi/10.1002/er.7782.

[28] Robin T. White, Sebastian H. Eberhardt, Yadvinder Singh, Tylynn Haddow, Monica Dutta, Francesco P. Orfino, Erik Kjeang, Four-dimensional joint visualization of electrode degradation and liquid water distribution inside operating polymer electrolyte fuel cells, Sci. Rep. (ISSN: 20452322) 9 (1) (2019) 1–12, http://dx.doi.org/10.1038/s41598-018-38464-9.

[29] Devashish Kulkarni, Stanley J. Normile, Liam G. Connolly, Iryna V. Zenyuk, Development of low temperature fuel cell holders for Operando X-ray micro and nano computed tomography to visualize water distribution, J. Phys.: Energy (ISSN: 2515-7655) 2 (4) (2020) 044005, http://dx.doi.org/10.1088/2515-7655/abb783, URL https://iopscience.iop.org/article/10.1088/2515-7655/abb783.

[30] Wiebke Maier, Tobias Arlt, Christoph Wannek, Ingo Manke, Heinrich Riesemeier, Philipp Krüger, Joachim Scholta, Werner Lehnert, John Banhart, Detlef Stolten, In-situ synchrotron X-ray radiography on high temperature polymer electrolyte fuel cells, Electrochem. Commun. (ISSN: 13882481) 12 (10) (2010) 1436–1438, http://dx.doi.org/10.1016/j.elecom.2010.08.002.

[31] R. Kuhn, J. Scholta, Ph Krüger, Ch Hartnig, W. Lehnert, T. Arlt, I. Manke, Measuring device for synchrotron X-ray imaging and first results of high temperature polymer electrolyte membrane fuel cells, J. Power Sources (ISSN: 03787753) 196 (12) (2011) 5231–5239, http://dx.doi.org/10.1016/j.jpowsour.2010.11.025.

[32] W. Maier, T. Arlt, K. Wippermann, C. Wannek, I. Manke, W. Lehnert, D. Stolten, Correlation of synchrotron X-ray radiography and electrochemical impedance spectroscopy for the investigation of HT-PEFCs, J. Electrochem. Soc. (ISSN: 0013-4651) 159 (8) (2012) F398–F404, http://dx.doi.org/10.1149/2.024208jes, URL https://iopscience.iop.org/article/10.1149/2.024208jes.

[33] S.H. Eberhardt, F. Marone, M. Stampanoni, F.N. Büchi, T.J. Schmidt, Quantifying phosphoric acid in high-temperature polymer electrolyte fuel cell components by X-ray tomographic microscopy, J. Synchrotron Radiat. (ISSN: 16005775) 21 (6) (2014) 1319–1326, http://dx.doi.org/10.1107/S1600577514016348.

[34] S.H. Eberhardt, F. Marone, M. Stampanoni, F.N. Buchi, T.J. Schmidt, Imaging phosphoric acid migration in high temperature polymer electrolyte fuel cells by X-Ray tomographic microscopy, ECS Trans. (ISSN: 1938-6737) 69 (17) (2015) 591–599, http://dx.doi.org/10.1149/06917.0591ecst,

[35] S.H. Eberhardt, F. Marone, M. Stampanoni, F.N. Büchi, T.J. Schmidt, Operando X-ray tomographic microscopy imaging of HT-PEFC: A comparative study of phosphoric acid electrolyte migration, J. Electrochem. Soc. (ISSN: 0013-4651) 163 (8) (2016) F842–F847, http://dx.doi.org/10.1149/2.0801608jes.

[36] N. Bevilacqua, M.G. George, S. Galbiati, A. Bazylak, R. Zeis, Phosphoric acid invasion in high temperature PEM fuel cell gas diffusion layers, Electrochim. Acta (ISSN: 00134686) 257 (2017) 89–98, http://dx.doi.org/10.1016/j.electacta.2017.10.054.

[37] S. Chevalier, M. Fazeli, F. Mack, S. Galbiati, I. Manke, A. Bazylak, R. Zeis, Role of the microporous layer in the redistribution of phosphoric acid in high temperature PEM fuel cell gas diffusion electrodes, Electrochim. Acta (ISSN: 00134686) 212 (2016) 187–194, http://dx.doi.org/10.1016/j.electacta.2016.06.121.

[38] Josh J. Bailey, Jianuo Chen, Jennifer Hack, Maria Perez-Page, Stuart M. Holmes, Dan J.L. Brett, Paul R. Shearing, Lab-based X-ray micro-computed tomography coupled with machine-learning segmentation to investigate phosphoric acid leaching in high-temperature polymer electrolyte fuel cells, J. Power Sources (ISSN: 03787753) 509 (August) (2021) 230347, http://dx.doi.org/10.1016/j.jpowsour.2021.230347.

[39] Anshuman Jakhmola, Nicolas Anton, Thierry F. Vandamme, Inorganic nanoparticles based contrast agents for X-ray computed tomography, Adv. Healthc. Mater. (ISSN: 21922640) 1 (4) (2012) 413–431, http://dx.doi.org/10.1002/adhm.201200032, URL https://onlinelibrary.wiley.com/doi/10.1002/adhm.201200032.

[40] Thomas M.M. Heenan, Chun Tan, Jennifer Hack, Dan J.L. Brett, Paul R. Shearing, Developments in X-ray tomography characterization for electrochemical devices, Mater. Today (ISSN: 18734103) 31 (December) (2019) 69–85, http://dx.doi.org/10.1016/j.mattod.2019.05.019.

[41] Victoria Manzi-Orezzoli, Adrian Mularczyk, Pavel Trtik, Jonathan Halter, Jens Eller, Thomas J. Schmidt, Pierre Boillat, Coating distribution analysis on gas diffusion layers for polymer electrolyte fuel cells by neutron and X-ray high-resolution tomography, ACS Omega (ISSN: 2470-1343) 4 (17) (2019) 17236–17243, http://dx.doi.org/10.1021/acsomega.9b01763, URL https://pubs.acs.org/doi/10.1021/acsomega.9b01763.

[42] Jing-Chie Lin, Chien-Ming Lai, Fu-Ping Ting, San-Der Chyou, Kan-Lin Hsueh, Influence of hot-pressing temperature on the performance of PEMFC and catalytic activity, J. Appl. Electrochem. (ISSN: 0021-891X) 39 (7) (2009) 1067–1073, http://dx.doi.org/10.1007/s10800-008-9758-1, URL http://link.springer.com/10.1007/s10800-008-9758-1.

[43] Q. Meyer, N. Mansor, F. Iacoviello, P.L. Cullen, R. Jervis, D. Finegan, C. Tan, J. Bailey, P.R. Shearing, D.J.L. Brett, Investigation of hot pressed polymer electrolyte fuel cell assemblies via X-ray computed tomography, Electrochim. Acta (ISSN: 00134686) 242 (2017) 125–136, http://dx.doi.org/10.1016/j.electacta.2017.05.028.

[44] Jennifer Hack, T.M.M. Heenan, F. Iacoviello, N. Mansor, Q. Meyer, P. Shearing, N. Brandon, D.J.L. Brett, A structure and durability comparison of membrane electrode assembly fabrication methods: Self-assembled versus hot-pressed, J. Electrochem. Soc. (ISSN: 0013-4651) 165 (6) (2018) F3045–F3052, http://dx.doi.org/10.1149/2.0051806jes, URL https://iopscience.iop.org/article/10.1149/2.0051806jes.

[45] Christoph Wannek, Irene Konradi, Jürgen Mergel, Werner Lehnert, Redistribution of phosphoric acid in membrane electrode assemblies for high-temperature polymer electrolyte fuel cells, Int. J. Hydrogen Energy (ISSN: 03603199) 34 (23) (2009) 9479–9485, http://dx.doi.org/10.1016/j.ijhydene.2009.09.076.

[46] I. Akkurt, B. Mavi, A. Akkurt, C. Basyigit, S. Kilincarslan, H.A. Yalim, Study on dependence of partial and total mass attenuation coefficients, J. Quant. Spectrosc. Radiat. Transfer (ISSN: 00224073) 94 (3–4) (2005) 379–385, http://dx.doi.org/10.1016/j.jqsrt.2004.09.024, URL https://linkinghub.elsevier.com/retrieve/pii/S0022407304004315.

[47] Jennifer Hack, Pablo A. García-Salaberri, Matthew D.R. Kok, Rhodri Jervis, Paul R. Shearing, Nigel Brandon, Dan J.L. Brett, X-ray micro-computed tomography of polymer electrolyte fuel cells: What is the Representative Elementary Area? J. Electrochem. Soc. (ISSN: 0013-4651) 167 (1) (2020) 013545, http://dx.doi.org/10.1149/1945-7111/ab6983.

[48] Justo Lobato, Pablo Cañizares, Manuel A. Rodrigo, F. Javier Pinar, Diego Úbeda, Study of flow channel geometry using current distribution measurement in a high temperature polymer electrolyte membrane fuel cell, J. Power Sources (ISSN: 03787753) 196 (9) (2011) 4209–4217, http://dx.doi.org/10.1016/j.jpowsour.2010.10.017.

[49] Jingjing Li, Linlin Yang, Hai Sun, Gongquan Sun, Comparative study of different activation procedures of high temperature proton exchange membrane fuel cells, Energy Technol. (ISSN: 2194-4288) 2100809 (2022) 2100809, http://dx.doi.org/10.1002/ente.202100809, URL https://onlinelibrary.wiley.com/doi/10.1002/ente.202100809.

[50] L.N. Cleemann, F. Buazar, Q. Li, J.O. Jensen, C. Pan, T. Steenberg, S. Dai, N.J. Bjerrum, Catalyst degradation in high temperature proton exchange membrane fuel cells based on acid doped polybenzimidazole membranes, Fuel Cells (5) (2013) 822–831, http://dx.doi.org/10.1002/fuce.201200186.

[51] Tonny Søndergaard, Lars Nilausen Cleemann, Lijie Zhong, Hans Becker, Thomas Steenberg, Hans Aage Hjuler, Larisa Seerup, Qingfeng Li, Jens Oluf Jensen, Catalyst degradation under potential cycling as an accelerated stress test for PBI-based high-temperature PEM fuel cells—Effect of humidification, Electrocatalysis (ISSN: 18685994) 9 (3) (2018) 302–313, http://dx.doi.org/10.1007/s12678-017-0427-1,

[52] Yağmur Özdemir, Nurhan Üregen, Yılser Devrim, Polybenzimidazole based nanocomposite membranes with enhanced proton conductivity for high temperature PEM fuel cells, Int. J. Hydrogen Energy (ISSN: 03603199) 42 (4) (2017) 2648–2657, http://dx.doi.org/10.1016/j.ijhydene.2016.04.132.